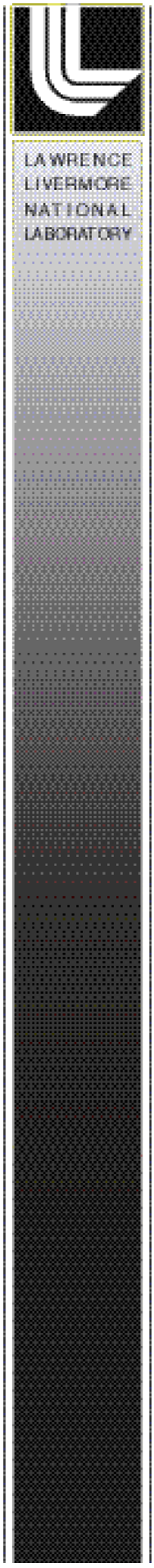

LLNL-CONF-466396

Fully Coupled Geomechanics and Discrete Flow Network Modeling of Hydraulic Fracturing for Geothermal Applications

P. Fu, S.M. Johnson, Y. Hao, and C. R. Carrigan.

Released on January 20, 2011

36th Annual Stanford Workshop on Geothermal Reservoir Engineering
Stanford, California, January 31 - February 2, 2011

Disclaimer

PROCEEDINGS, Thirty-Sixth Workshop on Geothermal Reservoir Engineering
Stanford University, Stanford, California, January 31 - February 2, 2011
SGP-TR-191

FULLY COUPLED GEOMECHANICS AND DISCRETE FLOW NETWORK MODELING OF HYDRAULIC FRACTURING FOR GEOTHERMAL APPLICATIONS

Pengcheng Fu, Scott M. Johnson, Yue Hao, and Charles R. Carrigan

Lawrence Livermore National Laboratory
7000 East Ave., L-286
Livermore, CA 94551, USA
e-mail: fu4@llnl.gov

ABSTRACT

The primary objective of our current research is to develop a computational test bed for evaluating borehole techniques to enhance fluid flow and heat transfer in enhanced geothermal systems (EGS). Simulating processes resulting in hydraulic fracturing and/or the remobilization of existing fractures, especially the interaction between propagating fractures and existing fractures, represents a critical goal of our project. To this end, we are continuing to develop a hydraulic fracturing simulation capability within the Livermore Distinct Element Code (LDEC), a combined FEM/DEM analysis code with explicit solid-fluid mechanics coupling. LDEC simulations start from an initial fracture distribution which can be stochastically generated or upscaled from the statistics of an actual fracture distribution. During the hydraulic stimulation process, LDEC tracks the propagation of fractures and other modifications to the fracture system. The output is transferred to the Non-isothermal Unsaturated Flow and Transport (NUFT) code to capture heat transfer and flow at the reservoir scale. This approach is intended to offer flexibility in the types of analyses we can perform, including evaluating the effects of different system heterogeneities on the heat extraction rate as well as seismicity associated with geothermal operations. This paper details the basic methodology of our approach. Two numerical examples showing the capability and effectiveness of our simulator are also presented.

INTRODUCTION

Engineered geothermal systems are created mainly through stimulation of lower permeability target formations using hydraulic fracturing to create or improve the subsurface heat exchanger component (MIT, 2006). As a prerequisite to the successful enhancement of permeability between the injection wells and the production wells, both the MIT study (2006) and DOE GTP panel express the need for guidance provided by credible hydraulic-fracturing stimulation models capable of addressing the propagation of clusters of fractures in hard rock.

While hydraulic fracturing has been in use for decades, understanding relatively complex fracture systems consisting of both pre-existing and newly created (by hydraulic stimulation) fractures remains a challenging task. A thorough review of the development of computer simulation techniques for hydraulic fracturing was provided by Adachi et al. (2007). Among the existing models/methods, the classic PKN and KGD models (Perkins and Kern, 1961; Geertsma and de Klerk 1969; Nordgren 1972) only handle the propagation of a single fracture with assumed simple geometries in a homogeneous medium. The pseudo-3D (P3D) and planar 3D (PL3D) models (Adachi et al. 2007) are capable of simulating fractures vertically extending through multiple geologic layers, but each simulation can only handle one crack lying in a single vertical plane. Although a number of models have emerged in recent years to explicitly simulate discrete fracture networks (e.g. McClure and Horne, 2010), the key mechanisms governing the interactions between the propagating new fractures and the existing fracture network, and the coupling between geomechanics and fluid dynamics, have not been rigorously included.

The principal objective of this work is to develop realistic computer-based models of EGS stimulation-response scenarios involving hydraulic stimulation of fracture systems in hard rock formations where a pre-existing fracture network may be present along with regional stress and temperature distributions. Our proposed approach is intended to assess the influence of many of the pertinent effects for EGS (e.g., formation mechanical characteristics, initial thermal and stress state of formation, hydraulic pumping parameters, etc.) on the time-dependent heat transfer capability of an initially low-permeability target formation. While much attention in the literature has been paid to exploring the local effects of stimulation near a single well bore, we aim to investigate how the stimulation of multiple wells, spaced across the reservoir, will influence heat transfer on a reservoir

scale by enhancing formation connectivity and permeability subject to realistic thermal and regional stress conditions. The ultimate goal of our work is to provide insight into selecting the best choices for producing long-term permeability enhancement on a site-by-site basis. This paper summarizes our initial research effort up to date, focusing on the development of numerical methods and the preliminary findings.

GENERAL APPROACH

Our current approach includes:

-A solid (geomechanics) solver, providing the non-local mechanical responses of the rock matrix;

-A flow solver, solving the fluid flow in inter-connected fracture networks;

- An adaptive remeshing module, generating new meshes for both the solid solver and the flow solver as fractures propagate;

- A rock joint model, determining hydraulic aperture sizes based on mechanical responses of the rock matrix as well as mechanical responses local to the fracture discontinuities.

Figure 1 shows how information is shared and exchanged between these modules in the simulator.

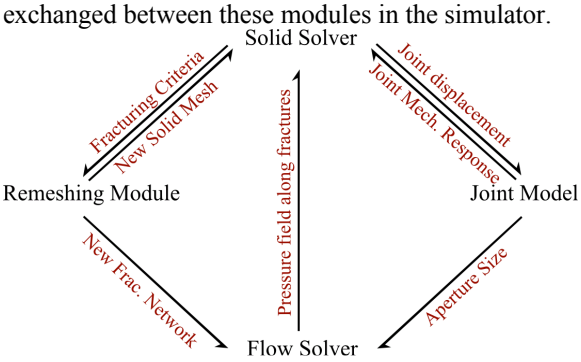

Figure 1: Important modules of the hydraulic fracturing simulator and information exchange between them in coupled simulations.

Ideally, a poroelasticity module is needed to consider the leak-off of fluid into the rock matrix along the fractures and the subsequent development of pore pressure. This module is among the features to be developed in our hydraulic fracturing simulator. However, in its current form, the simulator lacks the poroelasticity capability, so it is only suitable for simulating EGS in nearly impermeable rocks.

The Livermore Distinct Element Code (LDEC) is used as the basic platform, on which our hydraulic fracturing simulator is being developed. LDEC is a 3D computer code developed by the Computational Geosciences Group at LLNL to simulate the response of jointed geologic media to dynamic loading. Additional capabilities, including combined FEM-DEM analysis, fracture mechanics, and explicit solid-fluid coupling have been implemented in LDEC in the continued development over the past decade (Morris et al. 2006; Block et al. 2007; Johnson and Morris, 2009; Morris and Johnson, 2009).

The Non-isothermal Unsaturated Flow and Transport (NUFT), another LLNL code, is loosely (uni-directionally) coupled with LDEC to determine flow and transport at the reservoir scale; details can be found in Johnson et. al. (2004). NUFT has been developed to capture multiphase, multi-component heat and mass flow and reactive transport in unsaturated and saturated porous media (Nitao 1998). An integrated finite-difference spatial discretization scheme is used to solve mass and energy balance equations in both flow and reactive transport models. The resulting nonlinear equations are solved by the Newton-Raphson method. In our approach, the flow networks are characterized before and after hydraulic fracturing (as calculated in LDEC) and are homogenized into equivalent continuum properties (Johnson et al. 2010) for use in NUFT. NUFT is then used to evaluate the effects of the stimulation operation on heat transfer in the formation resulting from fracture enhanced permeability. An example of NUFT simulation results is shown in Figure 2.

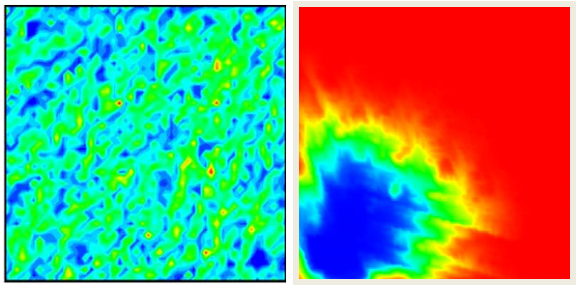

Figure 2: Example of NUFT simulation results: a permeability field (left) homogenized based on a discrete fracture network and temperature field (right) after certain period of heat production. (Conceptual demonstration not related to the numerical examples in this paper.)

Although the goal of our research project is to develop a three-dimensional hydraulic fracture capability and LDEC itself is a three-dimensional platform, the interim results in this paper are from the two-dimensional analogue. The two-dimensional interim model offers a simpler path to concept validation and provides a platform to optimize algorithms before migration to three dimensions. Most of the methods, algorithms, and phenomena

described in this paper apply to both two and three dimensions.

KEY MODULES

Solid Solver

The core of the solid mechanics solver is a conventional explicitly integrated finite element engine. Four-node tetrahedral elements and three-node plane strain triangle (the Turner triangle) elements are used in the three- and two-dimensional versions, respectively. A standard central-difference explicit time integration method is used, so the solver is inherently of a dynamic nature, although the mechanical responses of the rock matrix in the hydraulic fracturing process can be considered to be pseudo-static.

Flow Solver

Fluid flow in fracture networks is modeled with a modified finite volume method in LDEC. The formulation of the three-dimensional model was described by Johnson and Morris (2009). In this section we briefly present its two-dimensional analogue, the calculation of the critical time step, and a pumping boundary condition.

Finite volume methods employ either node-centered (vertex-centered) or element-centered (cell centered) formulations, and our model uses the latter. As shown in Figure 3, flow channels (corresponding to fracture networks in the solid phase) are discretized into inter-connected cells and are visualized as line segments. Note that the finite volume "elements" are termed as "cells" in this paper, and the term "element" is reserved for the solid solver to avoid confusion. For a given cell, i, a number of variables are defined, such as the length, L_i, fluid mass inside the cell, m_i, volume, V_i, fluid density, ρ_i, aperture size, α_i, fluid pressure, P_i, etc. Fluid is allowed to flow from one cell i to an adjacent cell j that is connected to cell i through a node. The permeability of the inter-cell interface is

$$\kappa_{ij} = \frac{\alpha_{ij}^3}{6\mu(L_i + L_j)} \qquad (1)$$

where μ is the dynamic viscosity of the fluid, and α_{ij} is the harmonic average (equation 2) of the apertures of the two adjacent cells i and j.

$$\alpha_{ij}^3 = \frac{\alpha_i^3 \alpha_j^3 (L_i + L_j)}{\alpha_i^3 L_j + \alpha_j^3 L_i} \qquad (2)$$

At each time step, fluid flow in and out each pair of connected cells is evaluated. For instance in Figure 3, four cells (2, 3, 5, and 6) are all connected to each other at node 3, and they constitute six i-j "pairs": 2-3, 2-5, 2-6, 3-5, 3-6, and 5-6. The inter-cell flow rate is calculated using equation (3).

$$\dot{V}_{ij} = \kappa_{ij}(P_j - P_i) \qquad (3)$$

The fluid is assumed to be compressible with a bulk modulus K. The fluid pressure in cell i is

$$P_i = \begin{cases} K(\rho_i / \rho_{ref} - 1) & \text{if } \rho_i > \rho_{ref} \\ 0 & \text{if } \rho_i \le \rho_{ref} \end{cases} \qquad (4)$$

where ρ_{ref} is the reference density of this fluid, corresponding to the density at zero or the datum pressure. As indicated by equation (4), the fluid pressure in a cell is assumed to be zero until the cell is completely filled with the fluid, which means that the vapor pressure is ignored and the gas phase is not considered. If the fluid is water, at 25°C, the three material parameters are:
$\mu = 8.90 \times 10^{-4}$ Pa·s,
$K = 2.2$ GPa, and
$\rho_{ref} = 1{,}000$ kg/m^3.

These three parameters are dependent on the temperature, and to a lesser extent, the pressure. Since the main purpose of this paper is to demonstrate simulation capabilities, rather than to simulate a specific EGS stimulation site, the above values are used in all the numerical examples unless otherwise indicated.

In spite of its simple format, this flow solver can sufficiently and effectively model the following two mechanisms important to simulating hydraulic fracturing: 1) flow in fracture networks due to pressure gradient; and 2) the conservation of fluid mass as the total volume of fractures varies (resulting from the creation of new fractures and the varying aperture sizes) with time. This solver lacks the capabilities of modeling certain other mechanisms, such as convection and sound wave propagation, but these mechanisms happen to be irrelevant to the phenomena and timescales that we intend to investigate.

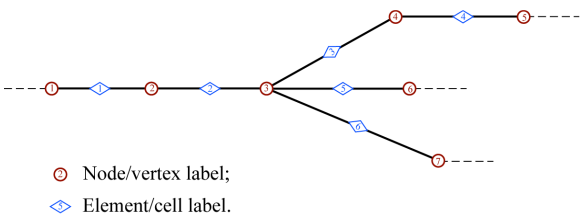

Figure 3: A simple flow network for demonstrating the finite volume formulation.

The flow system is solved using a central-difference explicit integration method. In each time step, the inter-cell flow is evaluated, and the state variables are

then updated. This approach is compatible with the solution method in the solid solver, enabling efficient coupling.

Pumping Boundary Condition

The fixed pressure and fixed flow rate boundary conditions for the flow solver have been described in Johnson and Morris (2009). In an actual hydraulic fracture operation, the flow boundary condition is neither of these two ideal conditions. Instead, a pump characteristic curve, which essentially describes the relationship between the pumping flow rate (q) and the pressure (or head, P_{pump}) that the pump can provide at this flow rate, exists for any given pump or pumping system. In this study, we use the following assumed pump curve.

$$P_{pump} = P_{\max}\left[1 - \frac{2}{\pi}\arctan\left(\frac{q}{q_{1/2}}\right)\right] \quad (5)$$

where P_{max} is the maximum pressure that this pump can provide at q=0, and $q_{1/2}$ is the flow rate when P_{pump}=0.5P_{max}. This form is selected in our model because it is easy to control the sensitivity of pumping pressure to flow rate by altering $q_{1/2}$, and also because the value of this function smoothly diminishes to zero as q increases, offering convenience to computer implementation. Nevertheless, any arbitrary pump curve can easily be substituted.

Time Stepping Considerations

The critical time step for the flow solver is

$$\Delta t_{flow\_crt} = \frac{6\mu}{K}\left(\frac{L_{ij}}{\alpha_{ij}}\right)^2 \quad (6)$$

Parameters μ, K, and L_{ij} are determined by the physical properties of the fluid phase and the characteristics of the meshing (domain discretization), and their values do not significantly change throughout a given simulation. On the other hand, the aperture sizes vary constantly as the hydraulic fracturing operation creates more fractures and the stress state of the matrix evolves. The largest aperture size in the system dictates the critical time step size and it typically increases as the operation progresses, so the critical time step tends towards a small value, which is a highly undesirable situation.

The solid solver also has a critical time step size and its value is the smallest mesh size divided by the sound speed in this solid medium. The critical time step for the solid solver is often a few orders of magnitude larger than the flow solver critical time step, and the smaller one of these two dictates a coupled analysis. Meanwhile, the computational cost of each time step for the solid solver is usually much higher than that for the flow solver. Consequently, if the solid solver and the fluid solver are coupled on a step-by-step basis, i.e., they exchange information every time step, the overall computational cost would be unacceptable, since the flow solver determines the total number of time steps (up to billions in a typical simulation) in a simulation and the solid solver determines the cost of each time step.

Our solution to this problem is to employ a "sub-stepping" scheme in the integration, using different step sizes for the two solvers. The time step for the solid solver is N (an integer) times larger than that for the flow solver. The two solvers interchange information after each solid solver time step and N steps in the flow solver. The time-varying aperture at each flow solver step is determined by extrapolation. As both the time step and the deformation of the rock matrix are very small, little error is induced by extrapolation. The average fluid pressure over the N time steps in the flow solver is fed into the solid solver as stress boundary conditions. This sub-stepping method has been found to greatly reduce the computational cost without impairing simulation accuracy and stability.

Fracturing Criterion

In the simulator, we use a discrete inter-element cohesive fracture approach similar to the methods proposed by Xu and Needleman (1994) and Camacho and Ortiz (1996). In such an approach, a fracturing criterion is specified, and the cohesive elements are invoked where this criterion is met. This type of fracturing criterion requires knowledge of the stress field near the fracture tip. However, our simulations typically cover a relatively large domain (up to hundreds of meters in each dimension) containing many existing fractures. It is impractical to use mesh sizes fine enough to obtain stress around the fracture tips with a very high resolution. To solve this problem, some features of the hydraulic fracturing phenomenon need to be considered.

In hydraulic fracturing, energy is consumed by three mechanisms, 1) viscous dissipation in the flow from the injection well to the leading edge of the fracture, 2) the work involved in fluid pressure acting perpendicularly to the fracture or potential fracture, and 3) energy transferred in creating new free surfaces. Depending on the relative significance of each of these mechanisms, a hydraulic fracturing process is often considered either "toughness-dominated" or "viscosity-dominated". For the latter case, energy dissipation in extending the fracture in the rock matrix is negligible compared to the dissipation due to viscous flow. Although toughness-dominated fracturing does exist under certain conditions (Detourna 2004), the phenomenon that we address, namely fracturing and fluid flow with the presence of complex fracture network, is almost always in the viscosity-dominated regime. Moreover, the compressive earth stress at typical depths for EGS

applications is usually one order of magnitude higher than the tensile strength of most rocks. Moderate error in predicting the net pressure (fluid pressure in excess of the earth pressure) required to extending fractures will only have minimal effects on the predicted pumping pressure and pressure distribution over the fracture network. In fact, most of the classic models for hydraulic fracturing assume that as soon as the fluid pressure at the leading edge of a fracture can overcome the compressive earth stress on this plane, the fracture will advance.

In light of these considerations, we find it acceptable to neglect the fine resolution of stress at the crack tip. The fracturing criterion we employ in the simulator is based on evaluating candidate fracture faces (lines segments in two dimensions), and these line segments overlap with finite element faces (edges in two dimensions) prior to surface formation. The criterion is expressed by equation (7):

$$\sigma_n \geq \lambda T_0 \qquad (7)$$

where σ_n is the normal stress (tension is positive) on the candidate fracture face (the interface between two adjacent elements in two dimensions), T_0 is the tensile strength of the rock, and λ is a mesh size-dependent correction factor, and the larger the mesh, the smaller the value of λ to account for the under-resolved stress at the crack tip due to large element sizes. We benefit from the monotonic trend of resolution on stress magnitude, i.e., magnitude increases with resolution up to very fine scales. In this study, since we are investigate a generic phenomenon common to many rock types instead of studying behaviors of a specific rock, we use λT_0=1.0MPa for all the numerical examples. Note that this kind of face-based method is different from the method in Camacho and Ortiz's (1996) original work and that in an earlier implementation of the cohesive element in LDEC by Block et al. (2007), which were both node-based.

All the potential fracture faces in the finite element mesh are repetitively checked against the criterion over the course of a simulation. Once this criterion is met, the face/edge is labeled as "fracture-ready". Before it can be split to create new fracture faces, certain geometrical conditions must be satisfied as discussed in the "Adaptive Remeshing" section.

Meshing

In finite element analysis of fracturing, fractures can only propagate along interfaces between adjacent elements. This limitation inevitably causes some mesh dependency of the simulation results. We use two meshing schemes as shown in Figure 4 to mitigate this problem. Figure 4(a) shows a regular grid consisting of triangles. In this configuration, a fracture can change the direction of propagation by 45° or 90°. In fact, this configuration is often used in fracture simulation (e.g. Xu and Needleman 1994) to minimize the restrictions on fracture propagation paths from the mesh. If some randomness in the propagation paths is desired, the location of each node is disturbed randomly to create meshes like that shown in Figure 4(b).

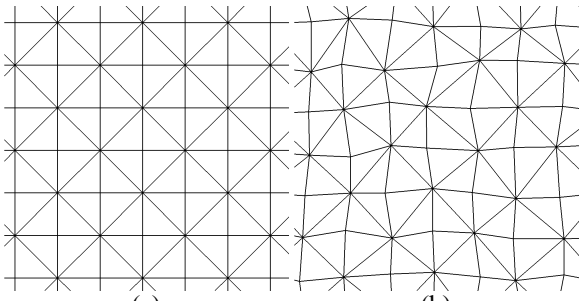

Figure 4: Typical mesh configurations.

Adaptive Remeshing

Although the fracturing criterion is based on faces/edges, in a finite element implementation it is impossible to split faces/edges without splitting nodes. In this section, we use an idealized example in Figure 5 to demonstrate the procedure of adaptive remeshing.

During a simulation, each time a fracture-ready edge is identified, the two nodes attached to this edge are examined. A node is usually attached to a number of edges. An edge is considered an "external edge" if there is only one element attached to it, while there are always two and only two elements attached to an "internal edge". An external edge either represents the free boundary the rock mass, or one of the faces along a fracture. A given node will be split if one the two following conditions are met:

1) Two of the edges connected to this node are fracture-ready;
2) One of the edges connected to this node is fracture-ready, and two of the edges are external.

For example, in the case shown in Figure 5(a), edge 8 and edge 13 have been identified as fracture ready. Subsequently, node 5 should be split because the first condition is satisfied (edges 8 and 13 are fracture-ready). Node 4 and node 9 also should be split since each of them has one fracture ready edge and two external edges attached, and the second condition is met.

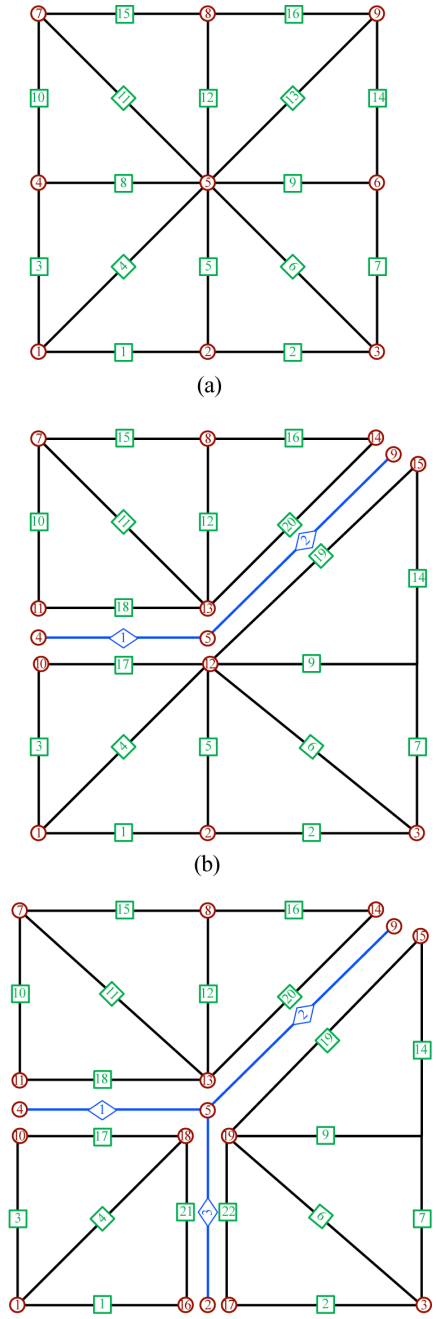

Figure 5: Adaptive remeshing of the finite element model to create new fractures. (a), (b), and (c) represent three states of the same mesh.

Figure 5(b) shows the mesh after the aforementioned remeshing has taken place. Each node that has been split generated two daughter nodes. For instance, nodes 12 and 13 are the daughter nodes of node 5. The daughter nodes belong to the new solid mesh while the mother nodes are detached from the solid mesh and attached to the newly created flow cells (cell 1 and cell 2). In a similar fashion, daughter edges are created for the new solid mesh while mother edges are converted into flow cells. Reusing the nodes and edges that have been detached from the solid mesh can ensure that intersecting fractures will result in correct connectivity of the new flow cells. For instance, edge 5 is identified to be fracture-ready at a later moment, and subsequently, node 12 and node 2 are split. The new flow cell (#3) should not be connected to node 12, which has just been split, but to node 5, the mother node of node 12 as shown in Figure 4(c).

During the remeshing process, the mapping between mother nodes and daughter nodes, and that between mother edges and daughter edges should be established and stored. Such information is used frequently during the simulation because we need to apply the fluid pressure in flow cells (which were all previously solid element edges) to their daughter edges as stress boundary conditions to the solid solver. On the other hand, the locations of the daughter nodes and daughter edges are used to update the locations of the flow cells and the aperture sizes.

Joint Model

Fractures are treated as fluid flow channels and mechanical joint elements in the flow solver and the solid solver, respectively. The mechanical responses of the joints directly impact the status of the flow channels, and most importantly, the hydraulic aperture sizes of the flow channels are determined based on certain characteristics of the corresponding joints.

In the solid solver, joints are represented by paired daughter edges. A contact model similar to those in the Distinct Element Method (or Discrete Element Method, DEM) is employed. As shown in Figure 6, edge p and edge q originate from the same mother edge, which is not shown. Edge p is geometrically characterized by its center point $\mathbf{x}_p$ in the vector form, its length L_p, a unit outer-pointing normal vector $\mathbf{n}_p$, and a unit tangential vector $\mathbf{t}_p$. Similar variables can be defined for edge q, and are not repeated here. The normal and tangential offsets between these two sister edges can be calculated as

$$\delta_n = (\mathbf{x}_q - \mathbf{x}_p) \cdot \mathbf{n}_p \quad (8)$$

$$\delta_t = (\mathbf{x}_q - \mathbf{x}_p) \cdot \mathbf{t}_p \quad (9)$$

When δ_n<0, the two elements that these two edges attached to geometrically penetrate into each other, representing the state that the two faces along the fracture are in contact. The normal contact force increment and the tangential contact force increment are calculated using the following equations:

$$\Delta F_n = K_n \dot{\delta}_n \Delta t \quad (10)$$

$$\Delta F_t = K_t \dot{\delta}_t \Delta t \qquad (11)$$

where K_n and K_t are the contact stiffnesses in the normal and tangential directions, respectively. Ideally, these two parameters are dependent on certain surface features of the rock body at the joint. In this study, we simply use the Young's modulus (20 GPa) and shear modulus (8.3 GPa) of the rock as K_n and K_t, respectively. In addition, Coulomb's law of friction with a friction angle of ϕ should be obeyed when calculating the tangential force based on its increment in each time step.

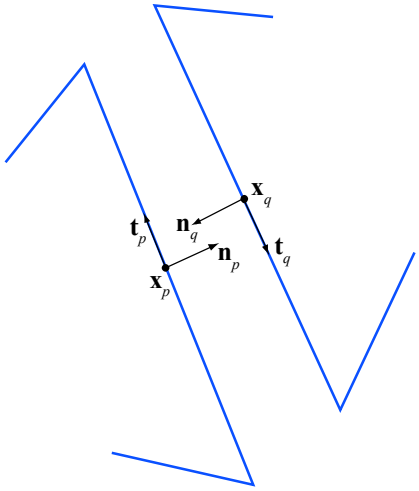

Figure 6: Relative position of two sister edges to demonstrate geometrical characteristics of a joint.

When δ_n>0, the two sister edges separate from each other by a gap, and δ_n is termed the geometrical aperture. The following equation (12) is used to calculate the hydraulic aperture.

$$\alpha = \begin{cases} \delta_n & if\ \delta_n > \alpha_r \\ \alpha_r & if\ \delta_n \le \alpha_r \end{cases} \qquad (12)$$

where α_r is called the "residual" aperture. α_r quantifies the residual flow conductivity of a closed fracture (i.e. the fluid pressure is not high enough to overcome the compressive rock stress) due to asperity of the fracture surface. Ideally, its value should be dependent on the normal stress acting on the fracture and dilation induced by shear deformation. We are researching and implementing more advanced joint models, such as the one proposed by Barton et al. (1985) to take these factors into account. However, the simplified model in equation (12) with assumed α_r=0.5 mm is used for the examples in this paper.

NUMERICAL EXAMPLE I - SIMULATION OF INTERACTION BETWEEN TWO FRACTURES: CROSS AND OFFSET

In this example, we simulate two mechanisms of interaction between a propagating fracture and a preexisting fracture in the perpendicular direction, that is the former crossing the latter, and the path of the former offsetting after intersecting the latter.

The simulation domain is 100 m long in both the x and y directions. Fixed deformation boundary conditions are applied to the four edges of the domain in the normal directions, while in the directions tangential to the boundaries the boundary nodes are free to move. The deformation boundary is such that homogeneous stress σ_{xx}=-20MPa and σ_{yy}=-10MPa is created if on fracture exists. Therefore, the y direction is the least compressive stress direction and fractures should have the tendency to propagate in the x direction. In this example, straight fractures are desired (not necessary though), so the mesh scheme shown in Figure 4(a) is adopted. The average mesh size is 1.0 m, so each model consists of 20,000 solid elements. Typical mechanical properties for rocks are used:
Young's modulus E=20 GPa,
Poisson's ratio ν=0.2, and
Tensile strength parameter λT_0=*1.0 MPa.*

The parameters pertaining to the flow solver have been provided in the "Flow Solver" section. The injection pump is located at x=0 and y=50m. The two pumping parameters are P_{max}=18MPa and $q_{1/2}$=2.0 m^3/s. Since $-\sigma_{xx}>P_{max}>-\sigma_{yy}$, under simple ideal boundary conditions, the pumping pressure is high enough to open fractures along the x direction, but not enough to open fractures along the y direction.

A preexisting fracture 10 meters long (from x=0 to 10m at y=50 m) was created and connected to the pumping point, which can be considered to be a perforation. The other preexisting fracture, 8 meters long was located at x=16m from y=46m to 54m as shown in Figure 7(a).

In the first simulation, the friction angle of the joint model is set to be 45°. After pumping commences, the fluid first infiltrates the preexisting fracture, resulting in development of pressure inside the fracture. When the pressure is high enough ($>-\sigma_{yy}$ =10MPa) to open the fracture, the aperture dilates, resulting in higher permeability. As expected, the fracture initially propagates horizontally. After it intersects the vertical fracture, the former "penetrates" through the latter and continues to propagate in the horizontal direction as shown in Figure 7(b). Note that the aperture size is magnified by twenty times to illustrate the distribution of the

aperture size along the fractures. The color depicts the fluid pressure distribution. The neighborhood around the intersection point is schematically shown in Figure 8 at the moment when the two fractures intersect but crossing has not yet taken place. As previously mentioned, the hydraulic pressure in the example is not high enough to open the vertical fracture, so the face *BC* remains in contact with *EF*, as do *B'C'* and *ED*. In Figure 8, these faces are plotted separately to illustrate contact stress along the joint. Owing to the fluid pressure in the horizontal fracture, block *ABC* moves upwards and block *A'B'C'* moves downwards, creating shear stress along the joint. This acts in opposite directions at the two sides of point *E* and creates tensile stress at point *E*, which in turn opens a new horizontal fracture at this point. This points to an interesting interpretation that the original crack tip does penetrate through the vertical fracture but rather disappears when the two fractures intersect, and a new fracture is initiated by the mechanism described above.

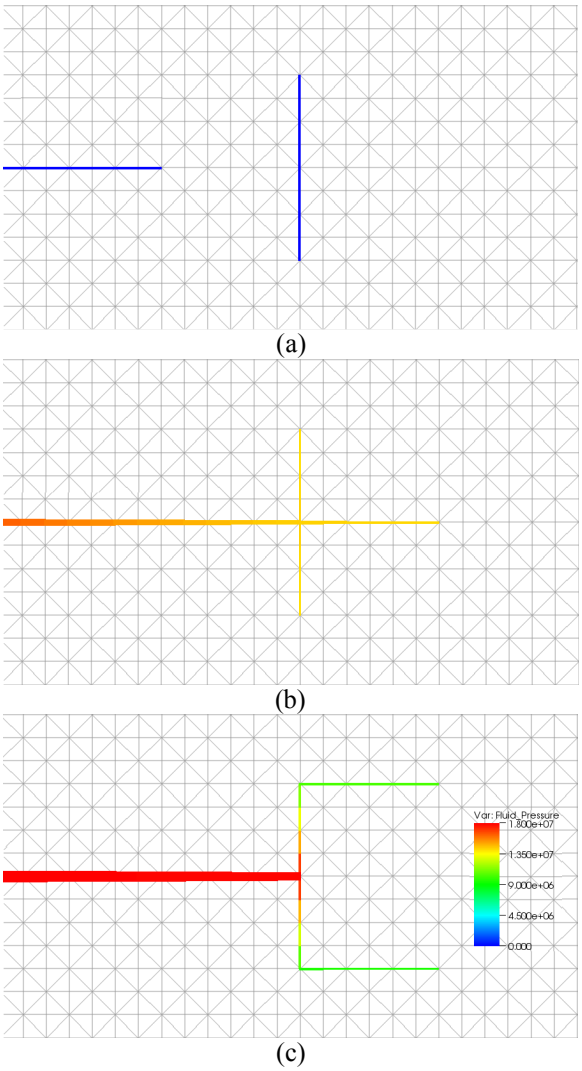

Figure 7: Interaction between two fractures. (a) The initial configuration; (b) crossing; and (c) offsetting.

To verify this mechanism, the joint friction angle is set to 3° in a parallel simulation, and the results are shown in Figure 7(c). After the horizontal fracture intersects the vertical one, no new fracture is created at point *E*. Instead, the fluid flows into the vertical fracture. Once the pressure reaches a critical value, new fractures initiate from the upper and lower tips of the vertical fracture and continue to propagate horizontally. Because the vertical fractures have much smaller apertures than their horizontal counterparts, the pressure drop is predominantly along the vertical direction.

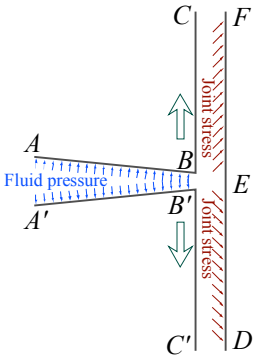

Figure 8: The mechanism of fracture crossing.

NUMERICAL EXAMPLE II - STIMULATION OF A PREEXISTING FRACTURE NETWORK

The simulation domain, the boundary conditions, as well as the pumping parameters are the same as those in the previous example. The domain can be considered as a horizontal cross-section of a reservoir. Here we seek to capture the behavior of a random fracture system, and the meshing scheme shown in Figure 4(b) with random nodal position disturbance is employed. The initial simulation domain including the preexisting fracture network is shown in Figure 9(a). The hydraulic fracturing operation with a maximum pumping pressure P_{max}=18 MPa and a duration of 60s has been simulated, and the new fracture network resulting from the stimulation is shown in Figure 9(b). By comparing the networks prior to and after hydraulic fracturing, it can be observed that new fractures are created at four locations as labeled in the figure. Note that Figure 9(b) is a snapshot at t=60s, when the high hydraulic pressure is still present in the domain, and therefore the "main branch" of the network has relatively large aperture sizes at this point. Also, the new fracture at point 4 is still extending, though, at a very slow rate.

We also use simulation to quantify the permeability enhancement of this fracture system resulting from hydraulic fracturing. Three production pressures (i.e. the pressure drop between the injection well and the production well) of 9 MPa, 12 MPa, and 15 MPa are investigated.

At a production pressure of 12 MPa, the flow rate distribution over the fracture network before the hydraulic fracturing operation is shown in Figure 10(a), and in Figure 10(b) for the network after hydraulic fracturing. It can be observed that new conducting branches parallel to the existing branches have been established. For instance, between x=5m and 30m, there are two branches in the new fracture system carrying significant flow compared to the one branch in the old network. The new branch running from x=45m to x=80m around y=55m seems to have taken a significant portion of the flow from a branch lower in the figure. The summary in Table 1 shows that the hydraulic fracturing operation has doubled or tripled the flow rate at each production pressure level. The flow rate on the new network appears to be more sensitive to pressure change than that of the original network.

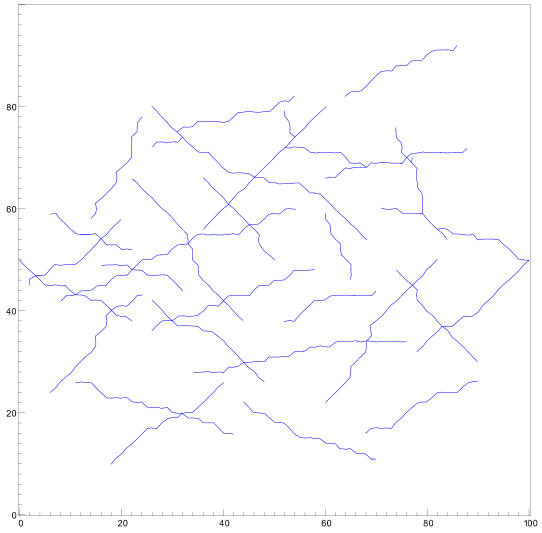

(a)

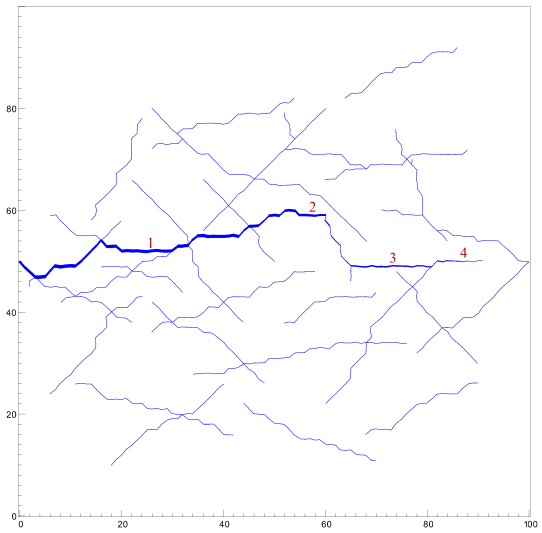

(b)

Figure 9: A random fracture network before (a) and after (b) hydraulic fracturing.

Table 1: Summary of flow rate improvement due to hydraulic fracturing.

	Flow rate (m^3/s per meter thickness)		
Production Pressure	9 MPa	12 MPa	15 MPa
Before Stimulation	0.00107	0.00149	0.00200
After Stimulation	0.00205	0.00315	0.00593

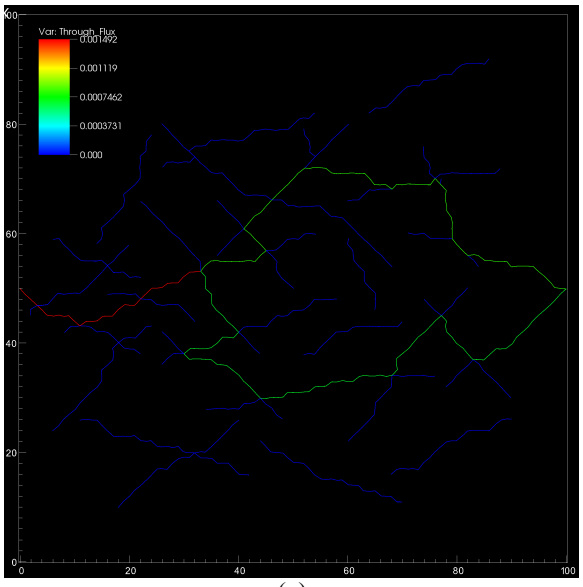

(a)

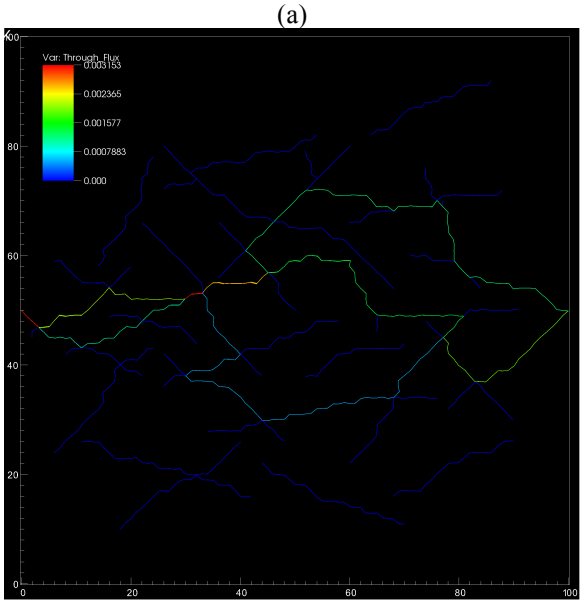

(b)

Figure 10: Flow rate distribution over the network (a) before and (b) after hydraulic fracturing. Note that the unit of the flow rate is m^3 per second per 1 m thick of the reservoir.

CONCLUDING REMARKS

In this paper we presented the basic simulation methodology for hydraulic fracturing that is being developed at the Lawrence Livermore National Laboratory. The approach features fully coupled geomechanics and discrete flow network modeling, and has the capability of simulating hydraulic fracturing in a relatively complex fracture network. The main algorithmic components of the simulator as well as the coupling strategy have been described. Two numerical examples are presented to demonstrate the basic capabilities of the approach. Our current and future work includes implementing the capabilities on a three-dimensional massively parallel platform and improving individual modules.

AUSPICES AND ACKNOLWEDGEMENTS

This work was performed under the auspices of the U.S. Department of Energy by Lawrence Livermore National Laboratory under Contract DE-AC52-07NA27344. Neither the United States government nor Lawrence Livermore National Security, LLC, nor any of their employees makes any warranty, expressed or implied, or assumes any legal liability or responsibility for the accuracy, completeness, or usefulness of any information, apparatus, product, or process disclosed, or represents that its use would not infringe privately owned rights. Reference herein to any specific commercial product, process, or service by trade name, trademark, manufacturer, or otherwise does not necessarily constitute or imply its endorsement, recommendation, or favoring by the United States government or Lawrence Livermore National Security, LLC. The views and opinions of authors expressed herein do not necessarily state or reflect those of the United States government or Lawrence Livermore National Security, LLC, and shall not be used for advertising or product endorsement purposes.

REFERENCES

The Future of Geothermal Energy: Impact of Enhanced Geothermal Systems (EGS) on the United States in the 21st Century (2006). Research report by an MIT-led interdisciplinary panel.

Adachi, J., Siebrits, E., Peirce, A., and Desroches J. (2007), "Computer simulation of hydraulic fractures," *International Journal of Rock Mechanics and Mining Sciences*, **44**, 739-757.

Barton, N., Bandis, S., and Bakhtar, K. (1985), "Strength, deformation and conductivity coupling of rock joints," *International Journal of Rock Mechanics and Mining Sciences & Geomechanics Abstracts*, **22**, 121-140.

Block, G., Rubin, M.B., Morris, J., and Berryman, J.G. (2007), "Simulations of dynamic crack propagation in brittle materials using nodal cohesive forces and continuum damage mechanics in the distinct element code LDEC," *International Journal of Fracture*, **144**, 131-147.

Camacho, G., and Ortiz, M. (1996), "Computational modelling of impact damage in brittle materials," *International Journal of Solids and Structures*, **33**, 2899-2938.

Detournay, E. (2004), "Propagation regimes of fluid-driven fractures in impermeable rocks," *International Journal of Geomechanics*, **4**, 35-45.

Geertsma, J., and de Klerk, F. (1969), "A rapid method of predicting width and extent of hydraulically induced fractures," *Journal of Petroleum Technology*, **21**, 1571-1581.

Huttert, K.M., and Willis, D.G. (1957), "Mechanics of hydraulic fracturing," *Transactions of The American Institute of Mining And Metallurgical Engineers*, **210**, 153-163.

Johnson, J.W., Nitao, J.J., and Knauss, K.G. (2004), "Reactive transport modeling of CO_2 storage in saline aquifers to elucidate fundamental processes, trapping mechanisms and sequestration partitioning", *Geological Storage of Carbon Dioxide*, S. J. Baines and R. H. Worden, Editors. Geological Society, London: London, 107-128.

Johnson, S.M., and Morris, J.P. (2009), "Modeling hydraulic fracturing for carbon sequestration applications," *the 43rd US Rock Mechanics Symposium and the 4th US-Canada Rock Mechanics Symposium*, Asheville, NC, ARMA 09-30.

Johnson, S.M., and Hao, Y. (2010), "Upscaling of thermal transport properties in enhanced geothermal systems" *Fall Meeting of the American Geophysical Union*, San Francisco, CA, Dec. 12-17.

McClure, M.W., and Horne, R.N. (2010), "Discrete fracture modeling of hydraulic stimulation in enhanced geothermal systems," *Proceedings of the 35th Workshop on Geothermal Reservoir Engineering*, SGP-TR-188.

Morris, J.P., Rubin, M.B., Block, G.I., and Bonner, M.P. (2006), "Simulations of fracture and fragmentation of geologic materials using combined FEM/DEM analysis," *International Journal of Impact Engineering*, **33**, 463-473.

Morris, J.P., and Johnson S.M. (2009), "Dynamic simulations of geological materials using combined FEM/DEM/SPH analysis,"

Geomechanics and Geoengineering: An International Journal, 4, 91-101.

Nitao, J.J. (1998), *Reference Manual for the NUFT Flow and Transport Code*, Version 2.0. Lawrence Livermore National Laboratory: Livermore, CA.

Nordgren, R.P. (1972), "Propagation of a vertical hydraulic fracture," *Society of Petroleum Engineers Journal*, **12**, 306-314.

Perkins, T.K., and Kern, L.R. (1961), "Widths of hydraulic fractures," *Journal of Petroleum Technology*, **13**, 937-949.

Xu, X.P., and Needleman, A. (1994), "Numerical simulations of fast crack growth in brittle solids," *Journal of the Mechanics and Physics of Solids*, **42**, 1397-1434.